batteries

MDPI

Article

Boosting the Capacitance of Aqueous Zinc-Ion Hybrid Capacitors by Engineering Hierarchical Porous Carbon Architecture

Yanzhen Li [1,†], Xin Zhang [1,†], Tong Lu [2], Ying Zhang [1], Xue Li [1], Dengfeng Yu [3,*] and Gongyuan Zhao [1,*]

[1] College of Chemistry, Chemical Engineering and Resource Utilization, Northeast Forestry University, 26 Hexing Road, Harbin 150040, China; liyanzhen202203@163.com (Y.L.); zhangxin20221015@163.com (X.Z.); zhangying20220307@163.com (Y.Z.); lixue2030@nefu.edu.cn (X.L.)
[2] Aulin College, Northeast Forestry University, 26 Hexing Road, Harbin 150040, China; atca19880107@163.com
[3] State Key Laboratory of New Ceramics and Fine Processing, School of Materials Science and Engineering, Tsinghua University, Beijing 100084, China
* Correspondence: hitydf@mail.tsinghua.edu.cn (D.Y.); zhaogy@nefu.edu.cn (G.Z.)
† These authors contributed equally to this work.

Abstract: With the merits of having excellent safety, being low cost and being environmentally friendly, zinc-ion hybrid supercapacitors (ZHSCs) are expected to be widely used in large-scale energy storage and flexible wearable devices. However, limited by their sluggish kinetic process, ZHSCs suffer from low-specific capacity and poor cycling stability at high cathode mass loading. Herein, a novel designed oxygen-rich hierarchical porous carbon (HPOC) is obtained by a one-step strategy of synchronous activation and templated for high-performance ZHSCs. The fabricated ZHSCs with HPOCs show significant improvement in Zn-ion storage capability, with a capacity of 209.4 mAh g^{-1} at 0.1 A g^{-1} and 108.3 mAh g^{-1} at 10 A g^{-1}. Additionally, the cycling stability is excellent, with 92.3% retention after 4000 cycles. Furthermore, an impressive areal capacity of 1.7 mAh cm^{-2} is achieved, even with a high mass loading of 12.5 mg cm^{-2}. More importantly, the flexible quasi-solid state ZHSCs also show a considerable capability (183.5 mAh g^{-1} at 0.1 A g^{-1}) and a high energy density of 178.0 Wh kg^{-1}. This promising result suggests a valuable route to produce functional nanocarbon materials for zinc storage applications.

Keywords: zinc-ion hybrid capacitors; hierarchical porous oxygen-rich carbon; quasi-state electrolyte; high-mass-loading cathode

Citation: Li, Y.; Zhang, X.; Lu, T.; Zhang, Y.; Li, X.; Yu, D.; Zhao, G. Boosting the Capacitance of Aqueous Zinc-Ion Hybrid Capacitors by Engineering Hierarchical Porous Carbon Architecture. *Batteries* **2023**, *9*, 429. https://doi.org/10.3390/batteries9080429

Academic Editor: Dino Tonti

Received: 26 June 2023
Revised: 28 July 2023
Accepted: 14 August 2023
Published: 17 August 2023

1. Introduction

Electrochemical energy storage technologies with high energy density and low cost hold high promise in portable electronic devices, vehicles and smart grid applications. Among various devices, lithium-ion batteries demonstrate considerable advantages in terms of their high energy density but fail to deliver fascinating power density [1–3]. Additionally, despite possessing an impressive power density (>10 kW kg^{-1}), supercapacitors (SCs) still face challenges in achieving satisfactory energy density [4–6]. Therefore, high-performance hybrid energy storage devices, combining the advantages of supercapacitors and batteries, have been widely explored. In particular, zinc-ion hybrid supercapacitors (ZHSCs) stand out among other emerging new energy storage devices with the benefits of abundant resources, high working voltages, good safety abilities and low manufacturing costs [7,8].

In general, ZHSCs are assembled with zinc-metal as an anode, porous capacitive materials such as a cathode and zinc salt-containing solutions, like $Zn(CF_3SO_3)_2$ and $ZnSO_4$ as an electrolyte [9–11]. They rely on similar principles employed in lithium metal batteries, i.e., Zn^{2+} stripping/deposition on the Zn metal anode and adsorption/desorption on the

cathode [12,13]. As the sluggish Zn-ion migration dynamics between Zn^{2+} and host materials dominate the Zn^{2+} storage kinetic process, the energy storage property of ZHSCs is limited to the adsorption/desorption capacity of cathodes to electrolyte ions [14,15]. Therefore, cathode materials are the critical factor in accommodating high-efficiency, stable and quickly charged Zn-ion storage devices. Carbonaceous materials offer several advantages compared to other cathode materials in ZHSCs. These advantages include their abundant availability at a low cost, high specific surface area, reasonable electronic conductivity, excellent electrochemical stability and the ability to tune their microstructure. Consequently, carbonaceous materials serve as an exemplary choice for cathode electrode materials in ZHSCs [16,17]. For example, Zhou et al. [18] found a two-step activation process using asphalt as a raw material and KOH as an activator to obtain the porous carbon with a high specific surface area of 3525.0 m^2 g^{-1}. The as-assembled ZHSC based on the porous carbon achieved a high specific capacity of 231.0 mAh g^{-1} at 0.5 A g^{-1}. Furthermore, Zou [19] reported a corn silks-derived carbon cathode that showed a high specific surface area (SSA) of 2441.0 m^2 g^{-1} and a high specific energy density of 38.5 Wh kg^{-1} at 14,741.0 W kg^{-1}.

Although some headway has been made in the application of high surface area activated carbon (AC) in ZHSCs, there are also serious limitations that cannot be ignored. First of all, AC-based cathodes exhibit inadequate ionic diffusion (typically around 10^{-13}–10^{-12} m^2 s^{-1}) at high current densities due to their microporous structure, compromising their potential for ultrafast long-life application [20–22]. Furthermore, inefficient utilization of the cathode's surface area arises from its poor wettability in an aqueous electrolyte, leading to low ionic transportation [23,24]. Moreover, vast amounts of chemical activating agents (usually four folds as the precursor), typically strong acids (like H_3PO_4) or alkalis (like NaOH and KOH) [25–27], are applied in the activation process, causing equipment corrosion and environment pollution. Therefore, it is a promising research direction to develop new types of carbon materials with developed pore structures, good wettability and high electrochemical properties for capacitors in a green way.

Herein, a novel one-step approach to synthesizing three-dimensional (3D) hierarchical porous oxygen-rich carbon (HPOC) from sodium carboxymethyl cellulose (CMC-Na) is reported. In this work, $KMnO_4$ is employed as both template and activator. As a consequence, the frame construction in the carbon product is fabricated by the in-built hard templates (MnO) and hierarchical porous formed on the frame resulting from the activation effect. Compared with the previous porous carbon, this work has several merits as below: (1) CMC-Na, derived from carboxymethylation of the hydroxyl group of cellulose obtained from various sources, is environmentally friendly and non-toxic. (2) O self-doping improves the wettability of porous carbon while creating extra active sites for zinc-ion adsorption and desorption. (3) Adding barely in a small amount, $KMnO_4$ cannot only introduce a hierarchical porous structure but also afford the in-built hard templates (MnO) to construct a 3D framework. Benefiting from the comprehensive modulation of the structure, hierarchical pores and surface chemistry, the obtained HPOC cathode provides significantly shortened ion transport distance and enhanced surface-activated sites. Consequently, the HPOC cathode-based ZHSCs demonstrate a high capacity of 209.4 mAh g^{-1} at 0.1 A g^{-1}, an ultrafast rate capability of 108.3 mAh g^{-1} at 10 A g^{-1}, a stable cycling life with retention of 92.3% after 4000 cycles and a high energy density of 178.0 Wh kg^{-1}. Furthermore, 71.7% of the initial capacity can be maintained under the mass loading of 12.5 mg cm^{-2} at 1 A g^{-1}. Moreover, HPOCs-based quasi-solid-state ZHSCs exhibited a high energy density of 157.1 Wh kg^{-1}, which presented potential applications in safe wearable electronics.

2. Materials and Methods

2.1. Chemicals

The following reagents are used, and no further purification is required. Sodium carboxymethyl cellulose (Shanghai McLean Biochemical Technology Co., Ltd., AR, Shanghai, China), $KMnO_4$ (Harbin Xinda Chemical Factory, AR, Harbin, China), gelatin (Shanghai Baiyan Technology Co., Ltd., AR, Shanghai, China), zinc sulfate heptahydrate ($ZnSO_4 \cdot 7H_2O$,

Shanghai Haohong Bio-medical Science and Technology Co., Ltd., AR, Shanghai, China), stainless steel wire mesh (Shanghai Weidi Metals Co., Ltd., 200 mesh, Shanghai, China), concentrated hydrochloric acid (Sinopharm Ltd., AR) and deionized (DI) water (Sinopharm Chemical Reagent Co., Ltd., AR, Shanghai, China).

2.2. Preparation of Hierarchical Porous Oxygen-Containing Carbon (HPOC)

Firstly, 2 g of CMC-Na was dissolved in 30 mL of deionized water and stirred under ambient temperature, then 1 g of $KMnO_4$ was added to the CMC-Na gel and stirred at a constant temperature of 80 °C in a water bath for 4 h. After that, the treated precursor was placed in a tube furnace and carbonized at 750 °C for 2 h in an argon atmosphere. Then, the carbon was washed with 3 M HCl and DI water until the pH was neutral and dry in a vacuum oven at 85 °C. After being dried, the final product was referred to as HPOC-1. As a control, the products obtained by direct carbonization of CMC-Na without any activator and 0.5 g of $KMnO_4$ were named HPOC-0 and HPOC-0.5, respectively.

2.3. Preparation of Flexible Gel Electrolyte for Solid-State-Battery

The experiment started by dissolving 2.9 g of $ZnSO_4 \cdot 7H_2O$ in 20 mL of DI water at room temperature. The solution was constantly stirred until it became transparent and uniform. Next, 2 g of gelatin was added to the solution and stirred at 60 °C for 30 min, resulting in a homogeneous sticky solution. The solution was then transferred to a glass dish and placed in a vacuum oven at 40 °C for 2 h. After this process, a transparent and flexible film was obtained from the sticky solution.

2.4. Structural Characterization

The crystalline properties of carbon materials were characterized by X-ray powder diffraction (XRD-6100, Shimadzu Corporation, Tokyo, Japan) and Raman spectrometry (Renishaw INVIA010410, London, UK). The morphology and structure of the samples were characterized by the scanning electron microscope (SEM, JSM-7500F, Japan Electronics Co., LTD, Tokyo, Japan) and the transmission electron microscope (TEM, JEM-2100 Japan Electronics Co., LTD, Tokyo, Japan). The composition of the elements and the surface state of carbon was analyzed by X-ray photoelectron spectroscopy (XPS, Thermo Scientific K-Alpha, Waltham, Massachusetts, USA). The SSA and pore size distribution of the carbon materials were determined using a nitrogen adsorption analyzer (ASAP-2460, Micromeritics instrument Ltd., Maryland, USA).

2.5. Electrochemical Measurements

The working electrode was obtained by mixing the synthesized carbon material and super P and Polytetrafluoroethylene (PTFE) in an ethanol solvent in a ratio of 8:1:1. To obtain the cathode, the stainless-steel mesh was coated with the mixed slurry and subjected to vacuum drying at 100 °C for 12 h. The mass loading of active materials on the cathode was approximately 1.0 mg cm^{-2}. The CR2025 battery consists of an aqueous 2.0 M $ZnSO_4$ electrolyte, a zinc foil anode, an active substance cathode and a Whatman (GF/D) glass fiber separator. The fabrication of the ZHSC and flexible Zn-ion hybrid supercapacitor (FZHS) differed slightly. Firstly, the Zn foil and the stainless-steel mesh were cut into a rectangle (20 × 15 mm). Secondly, the mixed slurry was coated on the stainless-steel mesh and acted as the cathode. Then the working electrode, flexible gel electrolyte and the Zn foil were assembled into the sandwich structure. To further improve the service life, the as-assembled ZHSC was further packaged with parafilm.

We conducted galvanostatic charge–discharge (GCD) and long cycle life experiments, as well as galvanostatic intermittent titration technique (GITT) tests, using a Neware BTS-4000 battery test system within the voltage range of 0.1–1.8 V. Additionally, cyclic voltammetry (CV) and electrochemical impedance spectroscopy (EIS) analyses were carried out on a Gammry Instruments electrochemical workstation (Reference 3000). The CV

measurements encompassed a voltage range of 0.1–1.8 V, while the EIS measurements were performed at 5 mV within the frequency range of 10^5–10^{-2} Hz.

3. Results

3.1. Material Characteristics

Scheme 1 represents the preparation process of HPOC samples. Generally, hierarchical porous oxygen-rich 3D carbon is likely attributed to the composition of CMC-Na and $KMnO_4$ treatment. Typically, along with the carbonization process, $KmnO_4$ decomposes into MnO and K_2CO_3 particles (Figure S1), and then K_2CO_3 decomposes into K_2O and CO_2. The multiple redox reactions generate substantial inner stress, inducing the formation of nanopores [28–30]. With the effect of MnO template and the following activation of K_2O in the carbon, a hierarchical porous 3D structure is obtained and confirmed by SEM. As shown in Figure 1a, by a simple direct-carbonization step, the pure CMC-Na removes the -COO-functional group [31] and introduces plenty of mesopores with a pore size range of 100–200 nm in the bulk structure, which provides an initial framework for $KMnO_4$ treatment. In consequence, the highly interconnected 3D porous carbon with numerous macropores and mesopores is obtained and displayed in Figure 1b–e. And, HPOC-1 shows a more developed pores structure. The elemental mapping of HPOC-1 in Figure 1f demonstrates the uniform distribution of carbon (C) and oxygen (O), suggesting uniform oxygen doping. The hierarchical pore structures of the HPOC-1 sample are clearly evident in the TEM images shown in Figure 1g,h. HPOC-1 exhibits an abundance of mesopores ranging from 5 to 30 nm in diameter, as well as a dense network of micropores (as depicted in the labeled region of Figure 1h,i). The presence of these numerous micropores and mesopores plays a significant role in achieving an ultra-high SSA, reducing ion transport distances and facilitating rapid charge transfer.

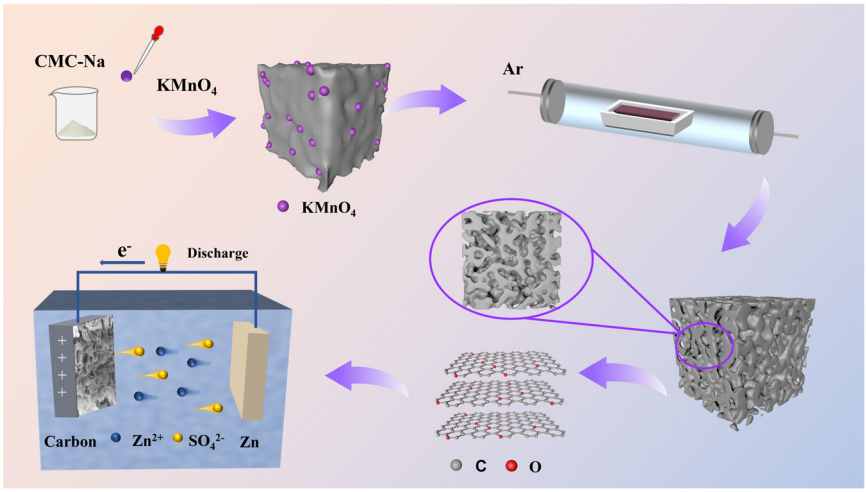

Scheme 1. Schematic illustration of the synthesis for HPOCs samples.

The disordered structure of HPOC samples was evaluated by Raman and XRD measurements. The two characteristic peaks at 1340 and 1580 cm^{-1}, corresponding to D-band and G-band can be observed in the Raman spectrum [32]. The intensity ratio of I_D/I_G is usually used to determine the graphitization degree for the carbon materials. As shown in Figure 2a, the calculated I_D/I_G values of HPOC-0, HPOC-0.5 and HPOC-1 are 1.0, 1.1 and 1.2, respectively. The content of defects/disorders in HPOC samples shows a typical amorphous state and HPOC-1 indicates a higher degree of graphitization, which reveals higher conductivity. The primarily disordered structures of all the HPOC samples are revealed by the wide and weak (002) peak, which was centered at approximately 25°, and the inconspicuous (100) peak found at 43°, as depicted in Figure 2b illustrating the XRD patterns of the HPOC-1 sample [27]. Moreover, the average thickness of the graphitic

domains, i.e., L_c, is calculated at about 1.2 nm based on the Scherrer equation ($L_c = \frac{k\lambda}{\beta \cdot \cos\theta}$, where $k = 0.89$, $\lambda = 0.15406$ nm, β is the half-height peak width and θ is the scattering angle), which is consistent with the HRTEM images (Figure S2).

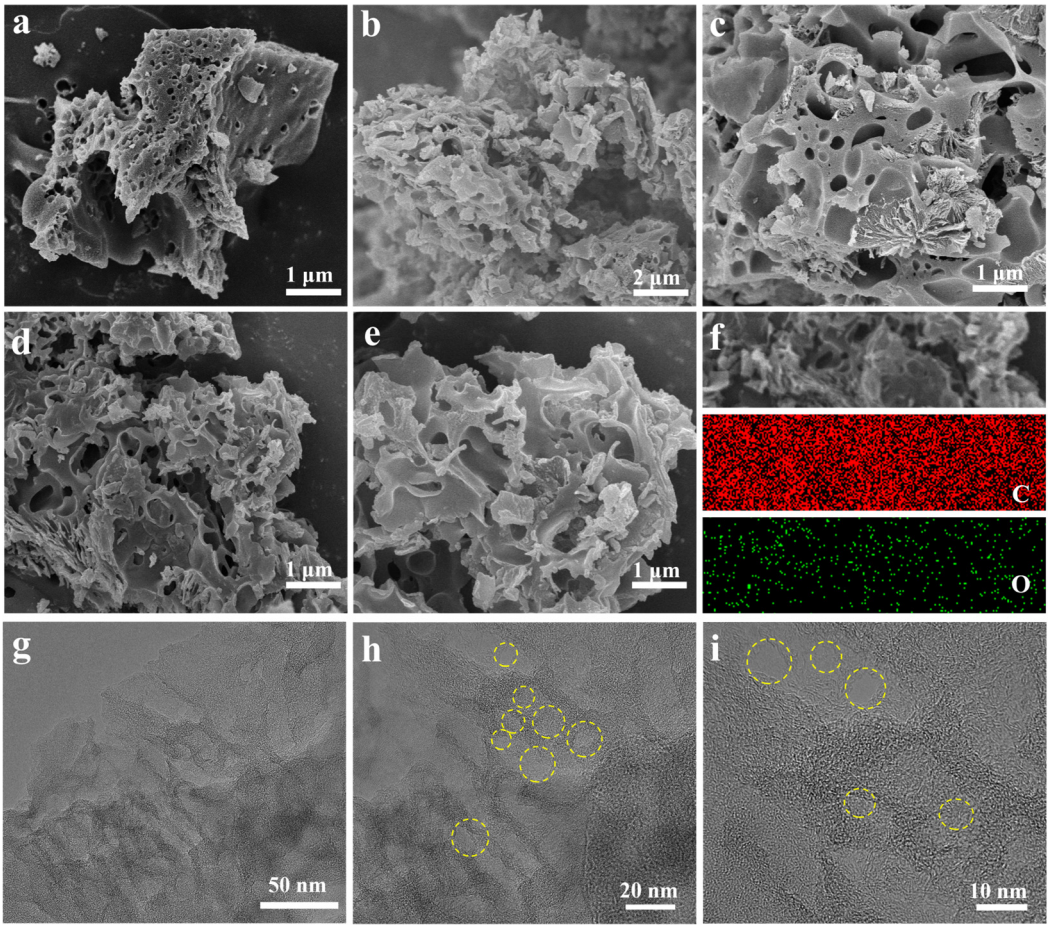

Figure 1. SEM images of (**a**) HPOC-0, (**b**,**c**) HPOC-0.5, (**d**,**e**) HPOC-1 and (**f**) Elemental mapping analysis of HPOC-1, (**g**,**h**) TEM images and (**i**) HRTEM images of HPOC-1.

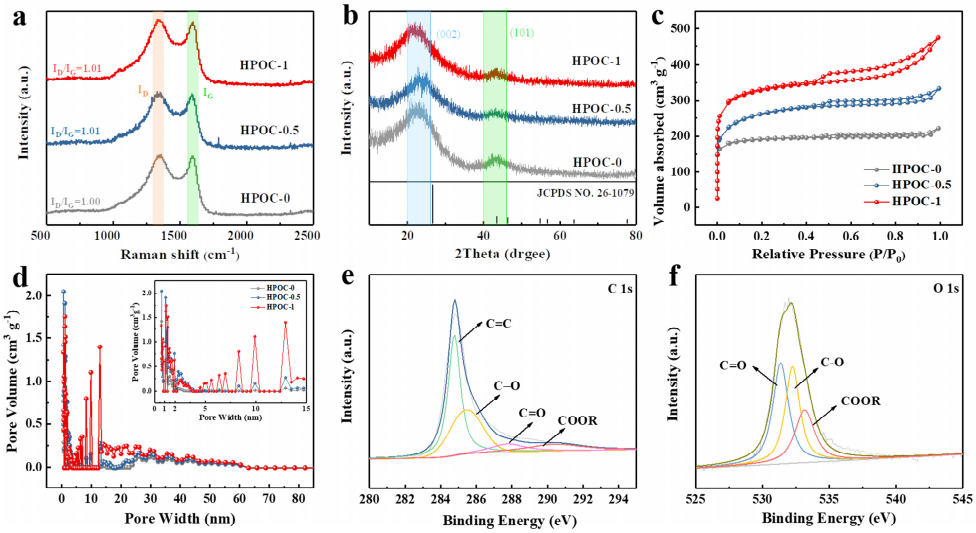

Figure 2. (**a**) Raman spectra, (**b**) XRD patterns, (**c**) N_2 absorption/desorption isotherms and (**d**) pore size distribution curves, (**e**) C 1s and (**f**) O 1s spectra of HPOC−1.

N_2 adsorption/desorption measurements were employed to further investigate the SSA and porous properties of HPOC samples. As shown in Figure 2c, HPOC samples presented a combination of Type I and Type IV N_2 adsorption–desorption isotherms with a rapid rise at low relative pressures ($P/P_0 < 0.05$), suggesting the existence of numerous micropores [33,34]. Moreover, we observed a noticeable hysteresis loop of the H4 type in the P/P_0 range of 0.5 to 0.9. This indicates the existence of hierarchical porosity in the HPOC-1 sample, which comprises mesopores and micropores, aligning with the previously mentioned TEM observations. Furthermore, we noticed a significant tail at higher pressures ($P/P_0 > 0.9$), suggesting the presence of macropores [35]. The SSA is shown in Table S1 and the SSA of HPOC-0, HPOC-0.5 and HPOC-1 are 606.1, 863.5 and 1071.5 $m^2\ g^{-1}$, respectively, which verify the pore-forming effect of $KMnO_4$ treatment. A more quantized hierarchically porous characteristic of HPOC samples can also be revealed by the pore size distributions in Figure 2d. A hierarchical porous structure is confirmed and micropores size is distributed at ≈0.6 nm and the mesopores size is centered at 2.2 and 36.3 nm.

In order to determine the composition of HPOC, XPS analysis was performed on the sample. The full XPS survey spectra in Figure S3 further verify the doping of O in the as-prepared HPOC-1. The oxygen content of HPOC-1 is 10.5%, superior to that of HPOC-0 (7.4%, Table S1), proving that $KMnO_4$ treating can introduce additional O elements. The C 1s spectra in Figure 2e are classified into four peaks located at 284.8, 285.5, 287.8 and 290.6 eV, corresponding to C=C, C-O, C=O and O-C=O, respectively [36]. The O 1s spectra (Figure 2f) are fitted into three individual peaks centered at 531.4, 532.3 and 533.2 eV, assigning to C=O, C-O and COOR [37]. According to prior research, the existence of oxygen atoms enhances the phenomenon of surface wetting and diminishes transfer resistance, thereby fostering an increase in capacitance output [38,39].

3.2. Electrochemical Properties of Aqueous HPOC//Zn System

In view of the 3D architecture, high SSA, abundant nanopores and the existing O-containing functional groups, HPOC is expected to deliver impressive electrochemical performance for ZHSCs. In order to evaluate the electrochemical performance of HPOC and its potential application, a two-electrode configuration using a 2 M $ZnSO_4$ electrolyte was fabricated. As shown in Figure 3a and Figure S4, an impressive rate capability was observed for HPOC-1 with values of 209.4, 173.7, 152.5, 137.5, 127.2, 116.1 and 108.3 mAh g^{-1} at 0.1, 0.2, 0.5, 1, 2, 5 and 10 A g^{-1}, surpassing that of HPOC-0 (56.8–32.7 mAh g^{-1}) and HPOC-0.5 (71.8–42.7 mAh g^{-1}). The porous structure's efficacy in enhancing energy storage and facilitating high-rate ion transport is affirmed by all the results, including a maintained specific capacitance of 75.0 mAh g^{-1} at 20 A·g^{-1} (Figure S5). As shown in Figure 3b, the GCD curves of HPOC-1 display a similar shape at different current densities, demonstrating good electrical conductivity and great electrochemical reversibility. A smaller IR drop can be confirmed in the GCD curves even at a high current density of 10 A g^{-1} (IR drop < 120.0 mV in 2 M $ZnSO_4$ solution), indicating a rapid electrochemical kinetic process.

To deepen the investigation into the impact of the hierarchical porous architecture on the transportation of electrolyte ions, we conducted EIS measurements. The equivalent circuit diagram of HPOC-1 is also given in Figure 3c, where Rs (0.3534 Ω) is the electrolyte interface impedance, R_{ct} (101.4 Ω) is the charge transfer resistance, W is the Warburg impedance for solid-phase diffusion and CPE is the double layer capacitance at the electrode/electrolyte interface. As shown in Figure 3c, among all samples, HPOC-1 demonstrates the lowest R_{ct} and R_w. The lowest R_{ct} and R_w further sustains that the porous structure of HPOC-1 and significantly promotes charge transfer and ion diffusion. The enhanced charge transfer and ion diffusion can reduce the severe electrode structural degradation upon repeated Zn^{2+} insertion/extraction. As a result, a high capacitance retention of 92.3% is achieved after 4000 charge–discharge cycles at a current density of 10 A g^{-1} (Figure 3d). The SEM images of the HPOC-1 electrode after 4000 cycles are given in Figure S6. After 4000 cycles, the structure and properties of HPOC electrodes remain

unchanged after the test, demonstrating the material's excellent stability. Owning to strong structural stability and fast Zn^{2+} kinetics, the hierarchical porous structure is still maintained. Obviously, the rate performance of HPOC-1cathodes is better than that of the majority reported carbon-based cathodes (Figure 3e) like mesoporous structured activated carbon (176.0 mAh g^{-1} at 0.1 A g^{-1}) [40], bamboo shaving derived porous carbon (88.0 mAh g^{-1} at 0.2 A g^{-1}) [41], glycerol derived mesopore-enriched carbon (114.4 mAh g^{-1} at 0.5 A g^{-1}) [42], B,N dual doped carbon (108.9 mAh g^{-1} at 1 A g^{-1}) [43] and honeycomb-like porous carbon (107.0 mAh g^{-1} at 5 A g^{-1}) [44].

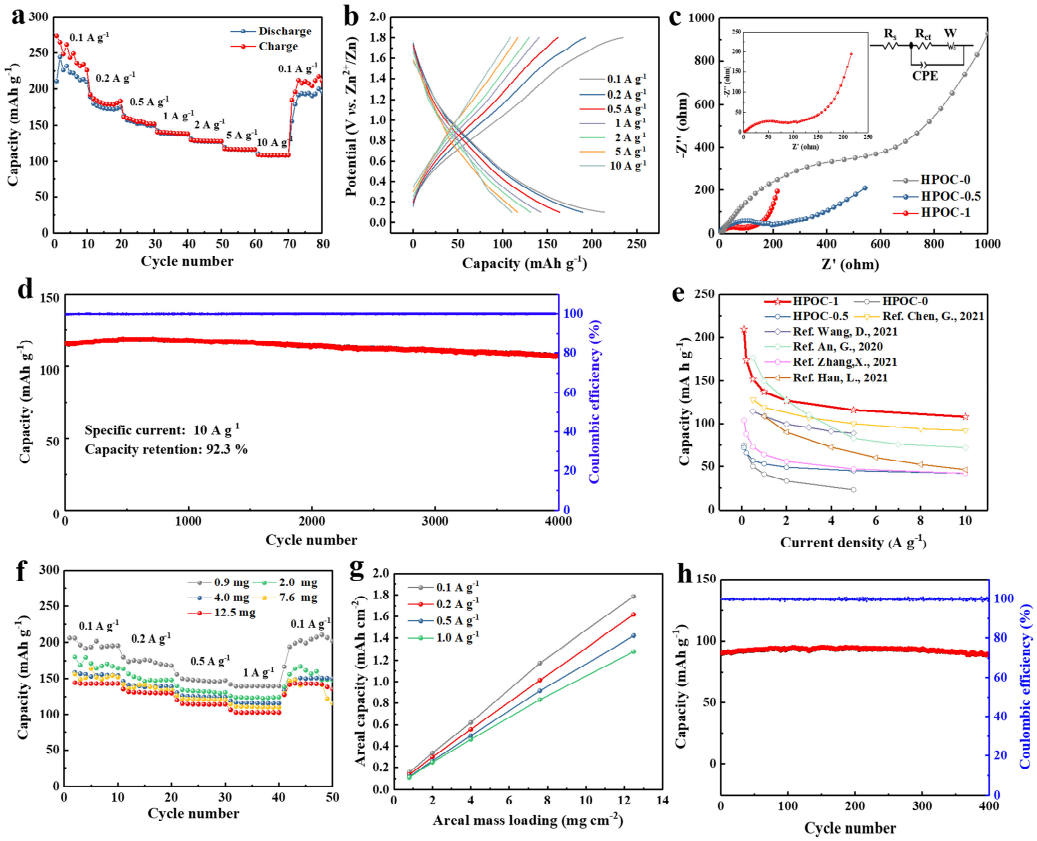

Figure 3. (**a**) Rate capability, (**b**) GCD profiles of the HPOC−1 electrode at different current densities, (**c**) Nyquist plots of HPOC−0, HPOC−0.5 and HPOC−1 (The inset shows an enlarged view of the Nyquist plots of the HPOC−1), (**d**) long cycle performance of HPOC−1 at 10 A g^{-1} for 4000 cycles, (**e**) Capacity comparison between HPOCs cathode and reported carbon electrodes [40–44], (**f**) the capacities of HPOC electrodes with different mass loading, (**g**) areal capacities of HPOC−1 with different mass loading and (**h**) cycling performance of HPOC−1 with high mass loading at 1 A g^{-1}.

In order to meet the demands of miniaturization in energy storage devices, there is an urgent need to develop electrode materials with high area capacities. With the advantages of hierarchical porous structure and high specific surface area, HPOC-1 shows outstanding electrochemical performance under low load, which is anticipated to overcome the issue of slow ion transport rate in high-load energy devices. Therefore, we carried out a series of tests of HPOC-1//Zn with different active mass loading of 0.9, 2.0, 4.0, 7.6 and 12.5 mg cm^{-2}. Encouragingly, outstanding rate performance is maintained under various loads and high capacities of 195.8, 164.8, 154.5, 152.0 and 143.1 mAh g^{-1} at 0.1 A g^{-1} are obtained (Figure 3f). The capacity loss is less than 2.1% even at a current density of 0.1 A g^{-1}. Additionally, Figure 3g showed that the areal capacity increases linearly with the mass loading, indicating a consistent trend even at high rates. By employing electrodes with a mass of 12.5 mg cm^{-2} at 1 A g^{-1}, ultrahigh areal capacities of 1.3 mAh cm^{-2} are achieved, which represents an 11.6-fold improvement over those observed for thin

electrodes (0.1 mAh cm^{-2} at 0.9 mg cm^{-2}). Additionally, electrodes of 11.6 mg cm^{-2} demonstrated a high capacity of 90.1 mAh g^{-1} and a consistent cycling life with 98.8% retention after 400 cycles in Figure 4h, indicating superb cycling stability and excellent kinetics response.

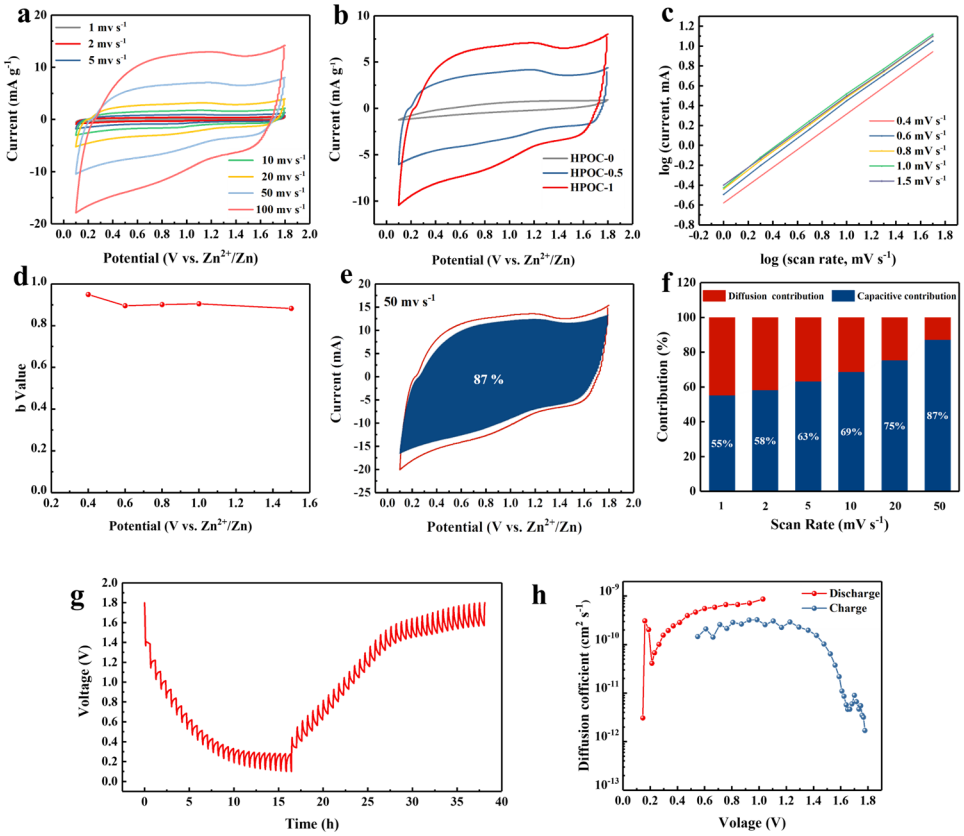

Figure 4. Electrochemical performance of Zn//HPOC−1. (**a**) CV curves at various scan rates (1–200 mV s^{-1}), (**b**) CV curves of the HPOCs at a scan rate of 50 mV s^{-1}, (**c**) b-values calculated by fitting the plots of log (current) vs. log (scan rate), (**d**) b-values at different potential, (**e**) the capacitive contributions at 50 mV s^{-1}, (**f**) capacitive contribution at different scan rates, (**g**) GITT curves for the Zn//HPOC−1 and (**h**) Zn^{2+} diffusion coefficient of HPOC−1 electrode.

The electrochemical kinetics of HPOC cathodes were investigated by cyclic voltammetry (CV) at scan rates ranging from 1 to 100 mV s^{-1} under the voltage window of 0.1—1.8 V. As shown in Figure 4a, the CV curves of HPOC-1 at various scan present quasi-rectangular shapes without obvious deformation, proving excellent structural stability and good reversibility. The slight bumps in the curve may be due to some redox reactions that occur during charge and discharge. The possible surface redox processes are as follow [24,45–47]:

$$> C - OH \Longleftrightarrow > C = O + H^+ + e^- , \quad (1)$$

$$-COOH \Longleftrightarrow > COO + H^+ + e^-, \quad (2)$$

$$> C = OH \Longleftrightarrow > C = O^-. \quad (3)$$

The CV curve of HPOC-1 cathodes in Figure 4b displays the biggest enclosed area, indicating the best electrochemical performance of the HPOC cathodes. Subsequently, the analysis of the electrochemical kinetics pertaining to the charge/discharge mechanism is carried out by examining the current response displayed by CV curves measured at various

scan rates. The observed peak current (i) maintains a proportional relationship with the scan rate (v) as follows:

$$i = av^b \text{ or } \log i = b\log v + \log a \,. \tag{4}$$

The kinetics for zinc ion storage can be identified by the values of b. If the b value approaches 0.5, the electrochemical behavior observed is predominantly capacitive. On the other hand, the b value close to 1 indicates diffusion behavior in the process [48–50]. As displayed in Figure 4c,d, the b values of HPOC-1 are 0.95, 0.89, 0.90 and 0.88 at the voltage of 0.4, 0.6, 0.8, 1.0 and 1.5 V, respectively, indicating the surface-controlled kinetics process is in dominated.

The capacitance and diffusion-controlled contributions are further calculated based on the following formula:

$$i = k_1 v + k_2 v^{\frac{1}{2}} \,, \tag{5}$$

where $k_1 v$ and $k_1 v^{\frac{1}{2}}$ represent the capacitance and diffusion-controlled process [38,51,52]. By calculating the k_1 and k_2 values at different voltages, the ratios of capacitive contribution could be quantitatively determined in Figure 4f. It can be seen intuitively that the contribution of the capacitive behavior increases from 55% to 99% at the different scan rates. Moreover, about 87% of the total capacity is originated from the surface capacitive contribution (blue region) at a scan rate of 50 $mV{\cdot}s^{-1}$, indicating that the surface-controlled capacity acts as a major capacity contributor at high scan rates. Furthermore, in order to quantitatively investigate the diffusion coefficient (D) of Zn^{2+} during the charging and discharging of the HPOC-1 electrode, the GITT test was applied (Figure 4g,h). The diffusion coefficient (D) was observed to be within the range of 10^{-9}~10^{-12} $cm^2\ s^{-1}$, suggesting a notably rapid ion migration rate attributed to the hierarchical porosity of HPOC. The diffusion coefficient of Zn^{2+} displayed a similar pattern of variation during the charge and discharge process, indicating that HPOC-1 electrode material possesses excellent reversibility in the process of zinc storage.

To investigate the charge storage mechanisms in more detail, we examined three specific states of the cathode: discharge to 1.2V (A), discharge to 0.1V (B), and charge to 1.2V (C). Additionally, we performed an ex situ XRD analysis of the HPOC-1, and the corresponding charge/discharge curve is presented in Figure 5a. The HPOC-1 electrodes were rinsed with deionized water before to characterization to remove the adsorbed $ZnSO_4$ electrolyte. As demonstrated in the XRD patterns in Figure 5b, at a discharge step from 1.6 to 0.1 V, peaks at 17.3°, 21.1°, 32.7°, 34.6° that corresponds to the (011), (110), (120) and (−311) plane of $Zn_4SO_4\ (OH)_6{\bullet}0.5H_2O$ (JCPDS. no 44-0674) is observed Therefore, we concluded that the following reactions occurred during the charging and discharging process [53]:

$$4Zn + 6OH^- + 0.5H_2O \longrightarrow ZnSO_4(OH)_6 \cdot 0.5H_2O \downarrow \,. \tag{6}$$

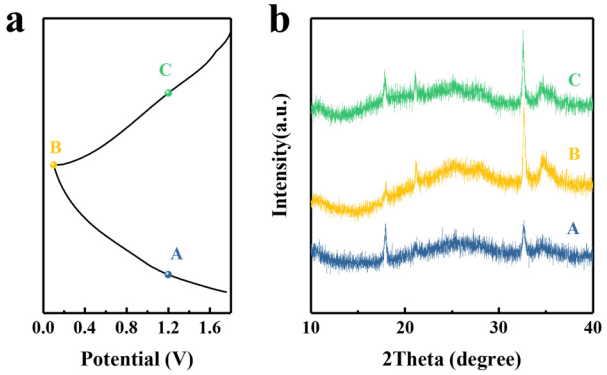

Figure 5. (**a**) Zinc storage mechanisms of Zn//HPOC-1 GCD curve at 0.1 A g^{-1} and (**b**) ex situ XRD of HPOC-1 sample at various states.

To exemplify the viability of this carbon material for practical applications, we assembled a quasi-solid-state device by employing gelatin gel as an electrolyte to realize the modularization of ZHSC (Figure 6a). Gelatin gel electrolyte is a typical kind of quasi-solid electrolyte, which is composed of liquid electrolyte ($ZnSO_4$ solution) and polymer matrix (gelatin gel) and has both the properties of liquid electrolyte and mechanical properties of solid polymer skeleton. Gelatin gel electrolyte can not only overcome the shortcomings of liquid electrolytes, such as easy leakage and difficult encapsulation, but also has high ionic conductivity of liquid electrolyte and good mechanical performance of solid electrolytes, therefore, showing a broad application prospect in portable electronic devices. Gelatin gel electrolytes are similar to liquid electrolytes in that it is zinc sulfate that plays a major role in the charging process. The self-discharging property is an important factor in determining the internal stability of energy storage systems. In this study, the zinc-ion hybrid capacitor was charged to 1.8 V and then left to rest for 80 h (Figure S7). The open-circuit potential stabilized at 1.25 V, and the self-discharge rate was measured to be 6.87 mV per hour, indicating a high level of stability. As shown in Figure 6b, HPOC-1 based-flexible zinc-ion hybrid supercapacitors (HPOC-1-FZHSCs) were evaluated at different current densities of 0.1, 0.2, 0.5, 1 and 2 A g^{-1} and exhibited the corresponding capacities of 183.5, 141.7, 107.8, 84.4 and 60.7 mAh g^{-1}. It can be concluded that the FZHSCs show a parallel electrochemical behavior and equivalent capacity to aqueous ZHSCs. Furthermore, the shapes of GCD curves are accordance with that of HPOC-1//Zn, and no obvious voltage plateau appears (Figure 6c), indicating a capacitive zinc ion storage behaviors. And, a high energy density of 157.1 Wh kg^{-1} and a high power density of 1696.9 W kg^{-1} are obtained. Long cycle performance of the as fabricated FZHSC was tested at 2 A g^{-1} and shown in Figure 6d. A capacitance retention rate of 85.5% and a coulombic efficiency of ~100% are obtained after 3000 cycles, indicating excellent cycling stability. More than that, with the high energy densities of 178.0 Wh kg^{-1} (HPOC-1//Zn) and 157.1 Wh kg^{-1} (HPOC-1-FZHSCs), HPOC-1 has an advantage over the other reported cathodes in ZHSCs such as PANI-derived activated carbon (101.0 Wh kg^{-1} at 67.8 W kg^{-1}) [54], honeycomb-like porous carbons (117.6 Wh kg^{-1} at 160.0 W kg^{-1}) [44], glycerol derived mesopore-enriched carbon nanosheets (160.0 Wh kg^{-1} at 106.4 W kg^{-1}) [42], N/P co-doped graphene (43.4 Wh kg^{-1} at 6750.0 W kg^{-1}) [55], O-doped porous carbon (69.4 Wh kg^{-1} at 7570.0 W kg^{-1}) [56], activated carbon (52.7 Wh kg^{-1} at 1725.0 W kg^{-1}) [57], N, O co-doped 2D carbon (94.6 Wh kg^{-1} at 449.9 W kg^{-1}) [58], N/O-codoped carbon nanofibrous (37.3 Wh kg^{-1} at 725.0 W kg^{-1}) [59] and oxygen-doped carbon network (12.3 Wh kg^{-1} at 99.7 W kg^{-1}) [60] as shown in Figure 6e and Table S3. These outstanding performances further verified the great potential of flexible ZHSCs as a flexible and wearable electronic product in the future.

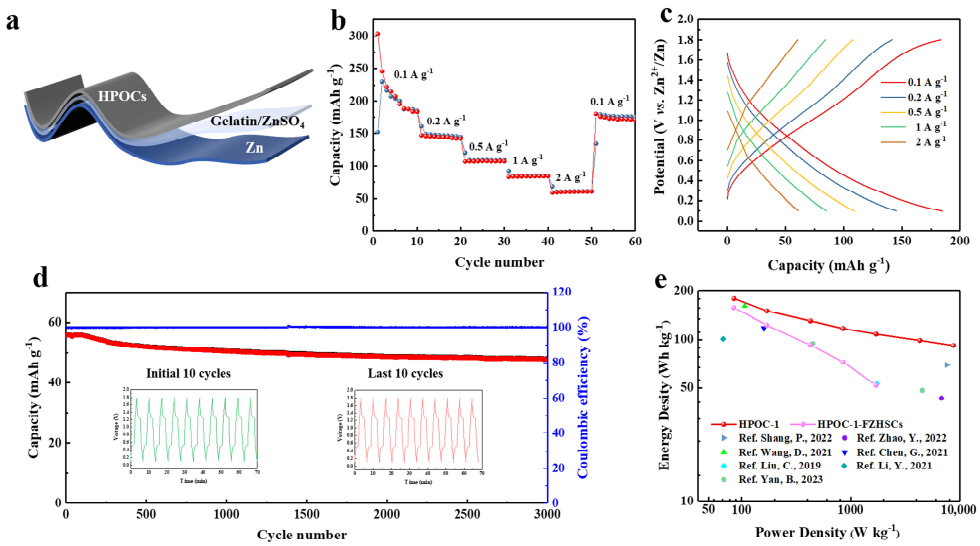

Figure 6. Electrochemical performance of the flexible ZHSCs (FZHSCs) device. (**a**) Schematic of the configuration of FZHSCs device, (**b**) Rate performance of HPOC-1−FZHSCs at 0.1–2 A g^{-1}, (**c**) corresponding GCD profiles, (**d**) cycling performance of HPOC-1−FZHSCs. at 2 A g^{-1} (the inset was the initial and last 10 GCD curves) and (**e**) ragone plots of HPOC−1-based ZHSCs and reported carbon-based ZHSCs [42,44,51–55].

4. Conclusions

In summary, we have designed a facile strategy to prepare a 3D hierarchical porous of framework oxygen-rich carbon using CMC as precursor and $KMnO_4$ as an activator. Benefiting from the high specific surface area, abundant oxygen functional groups, rich active sites and quick electron transfer, the optimized HPOC-1 presents high discharge capacities of 209.4 mAh g^{-1} at 0.1 A g^{-1} and maintains 108.3 mAh g^{-1} at 10 A g^{-1}. Furthermore, these ZHSCs exhibit a high energy density of 178.0 Wh kg^{-1}, high power density of 8698.8 W kg^{-1} and great cycle stability (the retention rate is 92.3% after 4000 cycles). Notably, even under high mass loading of 12.5 mg cm^{-2}, the ZHSCs also show superior rate properties and cycling stability over 4000 cycles. The HPOC-1-FZHSCs also present outstanding electrochemical performance, showing the potential in wearable devices.

Supplementary Materials: The following supporting information can be downloaded at: https://www.mdpi.com/article/10.3390/batteries9080429/s1, Figure S1: XRD patterns of HPOC@MnO (the sample after water washing and dried); Figure S2: HRTEM images of HPOC-1 sample; Table S1: Areal and pore distribution results of HPOC-0, HPOC-0.5 and HPOC-1; Figure S3: (a) Full XPS spectra of HPOC-0 and HPOC-1, (b) C1s, (c) O1s XPS spectra of HPOC-0; Table S2: he atomic content of C, O of carbon materials from the XPS result; Figure S4: (a) Rate capabilities of HPOC-0, HPOC-0.5, HPOC-1 cathodes at different current densities, (b) HPOC-0 and (c) HPOC-0.5 cycling performance at 10 A g^{-1}; Figure. S5: Gravimetric capacitances at different current densities of the HPOC-1 sample Figure S6: SEM image of HPOC-1 cathode after 4000 cycles; Figure S7: Self-discharge plots of FZHSCs and ZHSCs for HPOC-1 Table S3: Comparison of energy density and power density of various carbon-based supercapacitors from the references [55,61–70].

Author Contributions: Conceptualization, Y.L. and X.Z.; methodology, Y.Z.; software, X.Z.; validation, Y.L., T.L. and Y.Z.; formal analysis, X.L.; data curation, Y.L.; writing—original draft preparation, G.Z.; writing—review and editing, G.Z. and D.Y.; project administration, D.Y.; funding acquisition, G.Z. All authors have read and agreed to the published version of the manuscript.

Funding: This work was financially supported by Fundamental Research Funds for the Central Universities (2572022BU03), China Postdoctoral Science Foundation (2022M720690), Postdoctoral Foundation of Heilongjiang Province (LBH-Z22058) and College Students' Innovative Entrepreneurial Training Plan Program (202210225561).

Data Availability Statement: Data sharing not applicable.

Conflicts of Interest: The authors declare no conflict of interest.

References

1. Chen, Z.; Hsu, P.; Lopez, J. Fast and reversible thermoresponsive polymer switching materials for safer batteries. *Nat. Energy* **2016**, *1*, 15009. [CrossRef]
2. Li, Z.; An, Y.; Dong, S. Progress on zinc ion hybrid supercapacitors: Insights and challenges. *Energy Storage Mater.* **2020**, *31*, 252–266. [CrossRef]
3. Liu, Q.; Zhang, H.; Xie, J. Recent progress and challenges of carbon materials for zn-ion hybrid supercapacitors. *Carbon Energy* **2020**, *2*, 521–539. [CrossRef]
4. Su, L.; Gong, L.; Wang, X. Improved low-temperature performance of novel asymmetric supercapacitor with capacitor/battery-capacitor construction. *Int. J. Energy Res.* **2016**, *40*, 763–769. [CrossRef]
5. Dai, Y.; Liu, C.; Bai, Y. Framework materials for supercapacitors. *Nanotechnol. Rev.* **2022**, *11*, 1005–1046. [CrossRef]
6. Yin, J.; Zhang, W.; Alhebshi, N.A. Synthesis strategies of porous carbon for supercapacitor applications. *Small Methods* **2020**, *4*, 1900853. [CrossRef]
7. Tian, Y.; Zeng, G.; Rutt, A. Promises and challenges of next-generation "beyond li-ion" batteries for electric vehicles and grid decarbonization. *Chem. Rev.* **2021**, *121*, 1623–1669. [CrossRef] [PubMed]
8. Wang, H.; Zhu, C.; Chao, D. Nonaqueous hybrid lithium-ion and sodium-ion capacitors. *Adv. Mater.* **2017**, *29*, 1702093. [CrossRef]
9. Zhang, X.; Chen, C.; Gao, S. Graphene as regulating zinc deposition layer for long-life zinc ion hybrid supercapacitors. *J. Energy Storage* **2021**, *42*, 103037. [CrossRef]
10. Zhang, L.; Wu, D.; Wang, G. An aqueous zinc-ion hybrid super-capacitor for achieving ultrahigh-volumetric energy density. *Chin. Chem. Lett.* **2021**, *32*, 926–931. [CrossRef]
11. Li, Z.; Chen, D.; An, Y. Flexible and anti-freezing quasi-solid-state zinc ion hybrid supercapacitors based on pencil shavings derived porous carbon. *Energy Storage Mater.* **2020**, *28*, 307–314. [CrossRef]
12. Wang, T.; Li, S.; Weng, X.; Gao, L.; Yan, Y.; Zhang, N.; Qu, X.; Jiao, L.; Liu, Y. Ultrafast 3d hybrid-ion transport in porous cathodes for superior-rate rechargeable aqueous zinc batteries. *Adv. Energy Mater.* **2023**, *13*, 2204358. [CrossRef]
13. Sun, W.; Wang, F.; Hou, S. Zn/MnO_2 battery chemistry with H^+ and Zn^{2+} coinsertion. *J. Am. Chem. Soc.* **2017**, *139*, 9775–9778. [CrossRef] [PubMed]
14. Luo, X.; Chen, Y.; Mo, Y. A review of charge storage in porous carbon-based supercapacitors. *New Carbon Mater.* **2021**, *36*, 49–68. [CrossRef]
15. Ma, Q.; Xi, H.; Cui, F. Self-templating synthesis of hierarchical porous carbon with multi-heteroatom co-doping from tea waste for high-performance supercapacitor. *J. Energy Storage* **2022**, *45*, 103509. [CrossRef]
16. Dubal, D.P.; Ayyad, O.; Ruiz, V. Hybrid energy storage: The merging of battery and supercapacitor chemistries. *Chem. Soc. Rev.* **2015**, *44*, 1179–1777. [CrossRef] [PubMed]
17. Jha, S.; Akula, B.; Boddu, P. Roles of molecular structure of carbon-based materials in energy storage. *Mater. Today Sustain.* **2023**, *22*, 100375. [CrossRef]
18. Zhou, Z.; Zhou, X.; Zhang, M. In situ two-step activation strategy boosting hierarchical porous carbon cathode for an aqueous zn-based hybrid energy storage device with high capacity and ultra-long cycling life. *Small* **2020**, *16*, 2003174. [CrossRef]
19. Zou, Z.; Luo, X.; Wang, L. Highly mesoporous carbons derived from corn silks as high performance electrode materials of supercapacitors and zinc ion capacitors. *J. Energy Storage* **2021**, *44*, 103385. [CrossRef]
20. Zhang, L.; Zhang, F.; Yang, X. Porous 3D graphene-based bulk materials with exceptional high surface area and excellent conductivity for supercapacitors. *Sci. Rep.* **2013**, *3*, 1408. [CrossRef]
21. Lu, Y.; Zhang, S.; Yin, J. Mesoporous activated carbon materials with ultrahigh mesopore volume and effective specific surface area for high performance supercapacitors. *Carbon* **2017**, *124*, 64–71. [CrossRef]
22. Liu, J.; Wang, J.; Xu, C. Advanced energy storage devices: Basic principles, analytical methods, and rational materials design. *Adv. Sci.* **2018**, *5*, 1700322. [CrossRef] [PubMed]
23. Lu, Y.; Zhang, F.; Zhang, T. Synthesis and supercapacitor performance studies of n-doped graphene materials using o-phenylenediamine as the double-n precursor. *Carbon* **2013**, *63*, 508–516. [CrossRef]
24. Ghosh, S.; Barg, S.; Jeong, S.M. Heteroatom-doped and oxygen-functionalized nanocarbons for high-performance supercapacitors. *Adv. Energy Mater.* **2020**, *10*, 2001239. [CrossRef]
25. Su, H.; Lan, C.; Wang, Z. Controllable preparation of eucommia wood-derived mesoporous activated carbon as electrode materials for supercapacitors. *Polymers* **2023**, *15*, 663. [CrossRef] [PubMed]
26. Li, M.; Wang, Y.; Liu, Y. Preparation of active carbon through one-step naoh activation of coconut shell biomass for phenolic wastewater treatment. *Res. Chem. Intermed.* **2022**, *48*, 1665–1684. [CrossRef]
27. Zhu, X.; Yu, S.; Xu, K. Sustainable activated carbons from dead ginkgo leaves for supercapacitor electrode active materials. *Chem. Eng. Sci.* **2018**, *181*, 36–45. [CrossRef]
28. Becerra, M.E.; Arias, N.P.; Giraldo, O.H. Soot combustion manganese catalysts prepared by thermal decomposition of kmno4. *Appl. Catal. B Environ.* **2011**, *102*, 260–266. [CrossRef]

29. Lv, S.; Li, C.; Mi, J.; Meng, H. A functional activated carbon for efficient adsorption of phenol derived from pyrolysis of rice husk, koh-activation and edta-4na-modification. *Appl. Surf. Sci.* **2020**, *510*, 145425. [CrossRef]
30. Zhang, B.; Yang, D.; Qiu, X. Influences of aggregation behavior of lignin on the microstructure and adsorptive properties of lignin-derived porous carbons by potassium compound activation. *J. Ind. Eng. Chem.* **2020**, *82*, 220–227. [CrossRef]
31. Rahman, M.S.; Hasan, M.S.; Nitai, A.S. Recent developments of carboxymethyl cellulose. *Polymers* **2021**, *13*, 1345. [CrossRef] [PubMed]
32. Quan, H.; Tao, W.; Wang, Y. Enhanced supercapacitor performance of camellia oleifera shell derived hierarchical porous carbon by carbon quantum dots. *J. Energy Storage* **2022**, *55*, 105573. [CrossRef]
33. Bi, H.; He, X.; Zhang, H. N, p co-doped hierarchical porous carbon from rapeseed cake with enhanced supercapacitance. *Renew. Energy* **2021**, *170*, 188–196. [CrossRef]
34. Yuan, M.; Gao, M.; Shi, Q. Understanding the characteristics of water adsorption in zeolitic imidazolate framework-derived porous carbon materials. *Chem. Eng. J.* **2020**, *379*, 122412. [CrossRef]
35. Liu, X.; Zhu, H.; Gong, L. New insights into hierarchical pore size and level of concentration in efficient removal of toluene vapor by activated carbon. *Sci. Total Environ.* **2022**, *853*, 158719. [CrossRef]
36. Ma, T.; Liao, L.; Zhang, X. Hierarchical pores from microscale to macroscale boost ultrahigh lithium intercalation pseudocapacitance of biomass carbon. *J. Energy Storage* **2021**, *33*, 102068. [CrossRef]
37. Bai, Q.; Xiong, Q.; Li, C. Hierarchical porous carbons from a sodium alginate/bacterial cellulose composite for high-performance supercapacitor electrodes. *Appl. Surf. Sci.* **2018**, *455*, 795–807. [CrossRef]
38. Wang, H.; Chen, X.; Zhang, J. Unveiling the cooperative roles of pyrrolic-n and carboxyl groups in biomass-derived hierarchical porous carbon nanosheets for high energy-power zn-ion hybrid supercapacitors. *Appl. Surf. Sci.* **2022**, *598*, 153819. [CrossRef]
39. Huang, L.; Xiang, Y.; Luo, M. Hierarchically porous carbon with heteroatom doping for the application of Zn-ion capacitors. *Carbon* **2021**, *185*, 1–8. [CrossRef]
40. An, G. Ultrafast long-life zinc-ion hybrid supercapacitors constructed from mesoporous structured activated carbon. *Appl. Surf. Sci.* **2020**, *530*, 147220. [CrossRef]
41. Zhang, X.; Zhang, Y.; Zhang, H. Zinc-ion hybrid capacitor with high energy density constructed by bamboo shavings derived spongy-like porous carbon. *ChemistrySelect* **2021**, *6*, 6937–6943. [CrossRef]
42. Wang, D.; Pan, Z.; Chen, G. Glycerol derived mesopore-enriched hierarchically carbon nanosheets as the cathode for ultrafast zinc ion hybrid supercapacitor applications. *Electrochim. Acta* **2021**, *379*, 138170. [CrossRef]
43. Han, L.; Zhang, X.; Li, J. Enhanced energy storage of aqueous zinc-carbon hybrid supercapacitors via employing alkaline medium and b, n dual doped carbon cathode. *J. Colloid Interface Sci.* **2021**, *599*, 556–565. [CrossRef] [PubMed]
44. Chen, G.; Hu, Z.; Pan, Z. Design of honeycomb-like hierarchically porous carbons with engineered mesoporosity for aqueous zinc-ion hybrid supercapacitors applications. *J. Energy Storage* **2021**, *38*, 102534. [CrossRef]
45. Ding, B.; Guo, D.; Wang, Y. Functionalized graphene nanosheets decorated on carbon nanotubes networks for high performance supercapacitors. *J. Power Sources* **2018**, *398*, 113–119. [CrossRef]
46. Zhang, J.; Zhang, X.; Zhou, Y. Nitrogen-doped hierarchical porous carbon nanowhisker ensembles on carbon nanofiber for high-performance supercapacitors. *ACS Sustain. Chem. Eng.* **2014**, *2*, 1525–1533. [CrossRef]
47. Zhang, Q.; Yan, B.; Feng, L.; Zheng, J.; You, B.; Chen, J.; Zhao, X.; Zhang, C.; Jiang, S.; He, S. Progress in the use of organic potassium salts for the synthesis of porous carbon nanomaterials: Microstructure engineering for advanced supercapacitors. *Nanoscale* **2022**, *14*, 8216–8244. [CrossRef] [PubMed]
48. Dong, Y.; Li, Y.; Shi, H.; Qin, J.; Zheng, S.; He, R.; Wu, Z.-S. Graphene encapsulated iron nitrides confined in 3d carbon nanosheet frameworks for high-rate lithium ion batteries. *Carbon* **2020**, *159*, 213–220. [CrossRef]
49. Xu, H.; He, W.; Li, Z. Revisiting charge storage mechanism of reduced graphene oxide in zinc ion hybrid capacitor beyond the contribution of oxygen-containing groups. *Adv. Funct. Mater.* **2022**, *32*, 2111131. [CrossRef]
50. Deng, W.; Li, Y.; Xu, D.; Zhou, W.; Xiang, K.-X.; Chen, H. Three-dimensional hierarchically porous nitrogen-doped carbon from water hyacinth as selenium host for high-performance lithium–selenium batteries. *Rare Met.* **2022**, *41*, 3432–3445. [CrossRef]
51. Li, Y.; Yang, W.; Yang, W. Towards high-energy and anti-self-discharge Zn-ion hybrid supercapacitors with new understanding of the electrochemistry. *Nano-Micro Lett.* **2021**, *13*, 95. [CrossRef] [PubMed]
52. Yan, B.; Zheng, J.; Feng, L.; Zhang, Q.; Zhang, C.; Ding, Y.; Han, J.; Jiang, S.; He, S. Pore engineering: Structure-capacitance correlations for biomass-derived porous carbon materials. *Mater Des.* **2023**, *229*, 111904. [CrossRef]
53. Shang, P.; Liu, M.; Mei, Y. Urea-mediated monoliths made of nitrogen-enriched mesoporous carbon nanosheets for high-performance aqueous zinc ion hybrid capacitors. *Small* **2022**, *18*, 2108057. [CrossRef] [PubMed]
54. Liu, C.; Wu, J.C.; Zhou, H. Great enhancement of carbon energy storage through narrow pores and hydrogen-containing functional groups for aqueous zn-ion hybrid supercapacitor. *Molecules* **2019**, *24*, 2589. [CrossRef]
55. Zhao, Y.; Hao, H.; Song, T. High energy-power density zn-ion hybrid supercapacitors with n/p co-doped graphene cathode. *J. Power Sources* **2022**, *521*, 230941. [CrossRef]
56. Yu, J.; Wang, L.; Peng, J. O-doped porous carbon derived from biomass waste for high-performance zinc-ion hybrid supercapacitors. *Ionics* **2021**, *27*, 4495–4505. [CrossRef]
57. Wang, H.; Wang, M.; Tang, Y. A novel zinc-ion hybrid supercapacitor for long-life and low-cost energy storage applications. *Energy Storage Mater.* **2018**, *13*, 1–7. [CrossRef]

58. Lou, G.; Pei, G.; Wu, Y.; Lu, Y.; Wu, Y.; Zhu, X.; Pang, Y.; Shen, Z.; Wu, Q.; Fu, S.; et al. Combustion conversion of wood to N, O co-doped 2d carbon nanosheets for zinc-ion hybrid supercapacitors. *Chem. Eng. J.* **2021**, *413*, 127502. [CrossRef]
59. Yan, B.; Zheng, J.; Feng, L.; Zhang, Q.; Han, J.; Hou, H.; Zhang, C.; Ding, Y.; Jiang, S.; He, S. Green H_2O_2 activation of electrospun polyimide-based carbon nanofibers towards high-performance free-standing electrodes for supercapacitors. *Diam. Relat. Mater.* **2022**, *130*, 109465. [CrossRef]
60. Zheng, J.; Yan, B.; Feng, L.; Zhang, Q.; Zhang, C.; Yang, W.; Han, J.; Jiang, S.; He, S. Potassium citrate assisted synthesis of hierarchical porous carbon materials for high performance supercapacitors. *Diam. Relat. Mater.* **2022**, *128*, 109247. [CrossRef]
61. Shi, X.; Xie, J.; Yang, F. Compacting electric double layer enables carbon electrode with ultrahigh Zn ion storage capability. *Angew. Chem. Int. Ed.* **2022**, *61*, e202214773. [CrossRef] [PubMed]
62. Yu, P.; Zeng, Y.; Zeng, Y. Achieving high-energy-density and ultra-stable zinc-ion hybrid supercapacitors by engineering hierarchical porous carbon architecture. *Electrochim. Acta* **2019**, *327*, 134999. [CrossRef]
63. Chen, M.; Chen, J.; Zhou, W. High-performance flexible and self-healable quasisolid-state zinc-ion hybrid supercapacitor based on borax-crosslinked polyvinyl alcohol/nanocellulose hydrogel electrolyte. *J. Mater. Chem. A* **2019**, *7*, 26524. [CrossRef]
64. Shi, X.; Zhang, H.; Zeng, S.; Liu, X.; Lu, X. Pyrrolic-dominated nitrogen redox enhances reaction kinetics of pitch-derived carbon materials in aqueous zinc ion hybrid supercapacitors. *ACS Mater. Lett.* **2021**, *3*, 1291–1299. [CrossRef]
65. Liu, Z.; Li, G.; Cui, T. A battery-supercapacitor hybrid device composed of metallic zinc, a biodegradable ionic liquid electrolyte and graphite. *J. Solid State Electrochem.* **2018**, *22*, 91–101. [CrossRef]
66. Zheng, Y.; Zhao, W.; Jia, D. Porous carbon prepared via combustion and acid treatment as flexible zinc-ion capacitor electrode material. *Chem. Eng. J.* **2020**, *387*, 124161. [CrossRef]
67. Liu, H.; Chen, H.; Shi, K. Lignin-derived porous carbon for zinc-ion hybrid capacitor. *Ind. Crops Prod.* **2022**, *187*, 115519. [CrossRef]
68. Hui, J.; Yan, C.; Shi, Y. A biomass cathode derived from hyacinth bean for aqueous zinc-ion capacitors. *Ionics* **2022**, *28*, 1495–1499. [CrossRef]
69. Liu, L.; Lu, Y.; Qiu, D. Sodium alginate-derived porous carbon: Self-template carbonization mechanism and application in capacitive energy storage. *J. Colloid Interface Sci.* **2022**, *620*, 284–292. [CrossRef]
70. Liu, P.; Gao, Y.; Tan, Y.; Liu, W.; Huang, Y.; Yan, J.; Liu, K. Rational design of nitrogen doped hierarchical porous carbon for optimized zinc-ion hybrid supercapacitors. *Nano Res.* **2019**, *12*, 2835–2841. [CrossRef]